Optics and Lasers in Engineering 194 (2025) 109184

Contents lists available at ScienceDirect

Optics and Lasers in Engineering

journal homepage: www.elsevier.com/locate/optlaseng

Complex modulation Diffractive Optical Elements implemented in a single Spatial Light Modulator

Angela Soria-Garcia [a,*], Luis Miguel Sanchez-Brea [a], Jesus del Hoyo [a], Joaquin Andres-Porras [a,b], Javier Alda [b]

[a] Applied Optics Complutense Group, Department of Optics, Faculty of Physics, Universidad Complutense de Madrid, Plaza de las Ciencias 1, 28040, Madrid, Spain
[b] Applied Optics Complutense Group, Department of Optics, Faculty of Optics and Optometry, Universidad Complutense de Madrid, Calle Arcos de Jalón 118, 28037, Madrid, Spain

ARTICLE INFO

Keywords:
Spatial Light Modulators
Complex modulation
Distance-based iterative Fourier transform algorithm
Far-field diffraction
Diffractive Optical Elements

ABSTRACT

Spatial light modulators (SLMs) are optoelectronic devices that spatially modulate the properties of an incident electromagnetic field, such as its amplitude, phase, or polarization. They are used to generate dynamic Diffractive Optical Elements (DOEs), which are normally configured as pure-amplitude or pure-phase DOEs. In this work, we propose to generate complex modulation with a single SLM for optimizing the performance of DOEs. For that, we fill, as evenly as possible, the Argand plane, representing the complex amplitude of the DOE, with the modulation curve provided by the SLM and the polarization plates used. Also, we modify the Iterative Fourier Transform Algorithm to design complex DOEs and implement them in the SLM that works in an amplitude-phase configuration. For the simulations, we have considered that the modulation curves are spiral-shaped. We have verified that their far-field diffraction patterns present more uniformity, less background noise, and higher diffraction efficiencies than when pure-phase configuration is used. For the experimental verification, we have calibrated a LCoS SLM and optimized the azimuths of the polarizers and quarter-wave plates, placed before and after the SLM, to obtain the optimal modulation curve. The diffraction pattern generated by the studied complex DOEs presents a 32% increase in diffraction efficiency and a reduction of 85% in background noise compared to the phase DOE.

1. Introduction

Spatial Light Modulators are programmable devices that can control the intensity, phase, or polarization of light in a spatially varying manner. They have applications in many fields such as microscopy [1], quantum information processing [2], structured light [3], or beam shaping [4]. SLMs are commonly used in pure-phase or pure-amplitude configurations. Nevertheless, complex light modulation has gained importance as it is a powerful tool for many optical applications like holography [5], polarimetry [6], metasurfaces [7,8], and Vector Diffractive Optical Elements (VDOEs) [9], among others.

By adding polarizers and/or quarter waveplates, SLMs generate pure-amplitude or pure-phase DOEs. They are typically designed using the Iterative Fourier Transform Algorithm (IFTA). This algorithm, initially proposed by Gerchberg-Saxton [10], is used to generate DOEs that only modulate one property of light at a time, based on a desired far field intensity distribution. IFTA offers several advantages for design DOEs, such as computational efficiency and fast convergence. However, as it is a deterministic method, the solution is sensitive to the initial random seed, often leading to a local minimum rather than the global optimum. With the aim of increasing DOEs efficiency, several modifications to this algorithm have been suggested. One of the first modifications consisted of applying the algorithm's constrains to specific regions of the image to increase the degrees of freedom and, consequently, enhance the performance of the DOEs [11,12]. In addition, other variations of IFTA have been proposed, as the use of a relaxation parameter that controls the convergence rate [13,14], the combination of the IFTA with differential evolution algorithms [15,16], or the adaptation of the IFTA to the vector formalism [17]. Moreover, non-iterative approaches are also used for the efficient design of DOEs, using analytical phase encoding or direct calculations [18,19].

* Corresponding author.
E-mail address: angsoria@ucm.es (A. Soria-Garcia).

https://doi.org/10.1016/j.optlaseng.2025.109184
Received 20 May 2025; Received in revised form 19 June 2025; Accepted 23 June 2025
Available online 3 July 2025

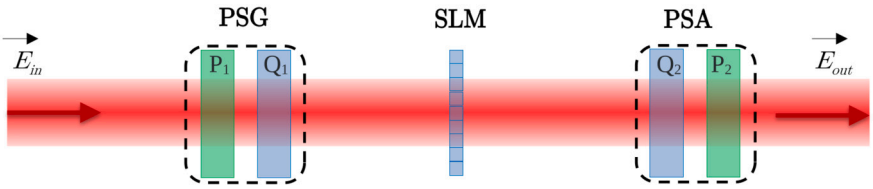

Fig. 1. Scheme for complex modulation with a transmission SLM.

For the generation of complex modulation with SLMs, several configurations have been explored. A common technique consists of combining two consecutive SLMs. For example, Lima et al. [20] optimized two displays independently for phase-only and amplitude-only configurations, respectively. However, the optimal configuration for each display individually may not be the optimal configuration when both displays are considered, meaning that they may not provide true amplitude and phase modulations. On the other hand, Bordakevich et al. [21] performed the optimization of the whole system to exploit its modulation capabilities. Since both works use two SLMs, the cost and difficulty of the set-up alignment increases, besides the fact that two different masks must be calculated. Double-pass SLM configuration is also used to achieve complex modulation. Macfaden [22] and Rosales-Guzman [23] proposed this technique dividing the SLM into two halves and performing a double-pass with a single SLM, respectively. These methods sacrifice resolution and also present alignment issues that can lead to cross-talk between pixels. Also, Hasegawa and Inoue [24] grouped several pixels together to achieve complex modulation, which reduces the effective resolution of the SLM.

In this work, we propose the use of complex modulation using a single SLM to improve the performance of dynamic DOEs implemented on SLMs. For that, we evenly fill the Argand plane, i.e., the amplitude-phase plane, with the modulation curve (MC) of the SLM. We calculated this MC from the Jones matrices of the SLM and the polarization plates placed before and after the SLM, whose azimuths are optimized using Particle Swarm Optimization (PSO) algorithm.

Since the modulation curve of the SLM is complex, we also propose a modification of IFTA algorithm, labeled as distance-based IFTA (D-IFTA), to design complex DOEs. This method minimizes the distances between the electric field of the DOE and the allowed values of the previously optimized MC of the SLM. This D-IFTA incorporates the MC of the SLM, facilitating the design of complex DOEs by efficiently exploiting the capabilities of the SLM. This contribution demonstrates, computationally and experimentally, how a complex modulation DOE can be realized using a single SLM. The optical set-up shows advantages over other methods, such as simplicity of alignment and no loss of resolution, allowing an easier integration of this type of DOEs.

2. Modulation curve of SLMs

Let us consider a LCoS SLM to implement dynamic DOEs. Since, its electro-optical mechanism changes the polarization properties of the incident light, each value of voltage (or grey level) can be modeled as a 2×2 Jones matrix, $\boldsymbol{J}_{SLM}(k)$, where $k = 1, \cdots, K$, and K is maximum grey level. Polarizers and retarders are used in combination with SLMs to transform this polarization modulation into phase or amplitude modulation. Fig. 1 shows an example of a modulation configuration with transmission SLMs. An incident circularly polarized light beam passes through the Polarization State Generator (PSG) formed by a linear polarizer, P_1, and a quarter wave-plate, Q_1, the SLM, and the Polarization State Analyzer (PSA), formed by a quarter wave-plate, Q_2, and a linear polarizer P_2. The emerging electric field after the set-up results in

$$\vec{E}_{\text{out}}(k,\vec{\theta}) = \boldsymbol{J}_{\text{PSA}}(\theta_{P_2},\theta_{Q_2}) \cdot \boldsymbol{J}_{\text{SLM}}(k) \cdot \boldsymbol{J}_{\text{PSG}}(\theta_{P_1},\theta_{Q_1}) \cdot \vec{E}_{\text{in}}\,, \tag{1}$$

where $\vec{E}_{in}$ represents the Jones vector of the input light,

$$\begin{aligned} \boldsymbol{J}_{\text{PSG}}(\theta_{P_1},\theta_{Q_1}) &= \boldsymbol{J}_{Q1}(\theta_{Q_1}) \cdot \boldsymbol{J}_{P1}(\theta_{P_1}), \\ \boldsymbol{J}_{\text{PSA}}(\theta_{P_2},\theta_{Q_2}) &= \boldsymbol{J}_{P2}(\theta_{P_2}) \cdot \boldsymbol{J}_{Q2}(\theta_{Q_2}), \end{aligned} \tag{2}$$

the symbol · corresponds with the matrix product, the parameters θ_{P_1}, θ_{Q_1}, θ_{Q_2}, and θ_{P_2} are the azimuths of the polarizing elements, and $\vec{\theta} = \left(\theta_{P_1},\theta_{Q_1},\theta_{Q_2},\theta_{P_2}\right)$ is a vector with the four azimuths to be determined.

Once the azimuths are fixed, the emerging electric field, $\vec{E}_{\text{out}}(k)$, corresponds to the modulation curve of our system, which can also be expressed as

$$\vec{E}_{\text{out}}(k) = \text{MC}[k]\vec{p} = A_k e^{i\phi_k}\vec{p}, \tag{3}$$

where $\vec{p}$ is an unitary linear polarization vector, which will be determined by P_2 and which is not relevant for most applications. Therefore, the shape of the MC depends on both the azimuths of the polarizers and quarter-wave plates of the PSG and PSA, and the Jones matrix of the SLM. For example, when phase modulation is required, the azimuths are selected so that $A_k \approx 1$ and $\phi_k \in (0, 2\pi]$. This means that the MC forms a circle in the Argand space. Moreover, other MCs are available by selecting the appropriate azimuths for the polarization plates.

3. Distance-based Iterative Fourier Transform Algorithm

The Iterative Fourier Transform Algorithm is commonly used to design DOEs for far field applications [25,26]. It determines the phase profile of a DOE to produce a target intensity distribution at the far field by using the Fast Fourier Transform (FFT) approach. As an initial seed, the algorithm uses a random phase and the amplitude of the target at the image plane. Then, the Inverse Fast Fourier Transform (IFFT) of the field is applied to determine the DOE, resulting in complex values, $\text{DOE}[i,j] = A_{ij}e^{i\phi_{ij}}$, where $i = 1, \cdots, M$ and $j = 1, \cdots, N$, being $M \times N$ the number of pixels of the DOE. This means that the mask should modulate both phase and amplitude at the same time. Since this is not normally possible with manufactured DOEs, restrictions on the DOE's modulation are applied. For example, for a phase DOE, the restriction imposes removing the amplitude modulation: $\text{DOE}[i,j] \rightarrow Ae^{i\phi_{ij}}$, where A is constant over the SLM. Next, the FFT is applied to the restricted DOE's field to obtain the diffraction pattern at the far field. As the first evaluation of the amplitude of the calculated field is usually very different than the desired target, the algorithm starts iterating between the DOE plane and the far field plane, using the last calculated phase distribution at the far field plane instead of a random one. The iterations continue until there is not further improvement in the far field distribution, obtaining the DOE's phase map as the final result.

When analyzing the Argand plane, the restrictions applied to the electric field for the phase DOE are quite hard, as it requires a large displacement, d_{ij}, for each pixel of the DOE to the phase MC, that is, the circle with radius 1, $A_k = 1$:

$$d_{ij} = \left\| A_{ij}e^{i\phi_{ij}} - A_k e^{i\phi_k} \right\| \approx \left\| A_{ij}e^{i\phi_{ij}} - e^{i\phi_{ij}} \right\| = 1 - A_{ij}, \tag{4}$$

where $\|\cdot\|$ represents the distance at the complex plane, $A_k \approx 1\ \forall k$, and $\phi_k \approx \phi_{ij}$, as long as the MC has enough sampling along the rim of the unit circle of the Argand plane.

Using the set-up of Fig. 1, a softer restriction than that of the pure-phase DOE, Eq. (4), is possible by filling the Argand plane with the SLM MC, Eq. (3), as evenly as possible, so that the displacements of the

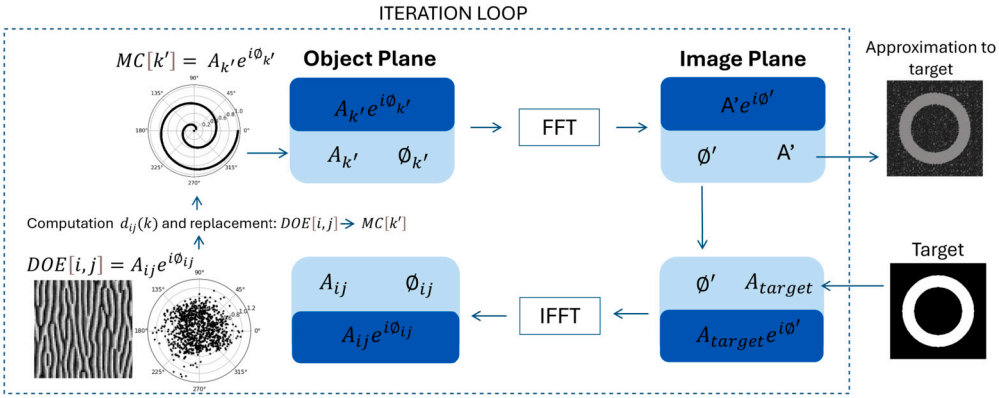

Fig. 2. Scheme of the D-IFTA used to design complex modulation DOEs.

DOE's field, DOE$[i,j]$, to MC$[k]$ are shorter. In this work, we propose a modification of the IFTA based on the minimization of the average displacements between DOE$[i,j]$, i.e., its amplitude and phase, and the MC$[k]$ produced by the SLM system. The distance-based IFTA also uses the FFT and IFFT to propagate the electric field between the object and image plane, and applies amplitude constrains in the image plane. However, in the object plane, we calculate the distance between the electric field of the DOE with each point of the constrain modulation curve,

$$d_{ij}(k) = \|\text{DOE}[i,j] - \text{MC}[k]\| = \left\| A_{ij}e^{i\phi_{ij}} - A_k e^{i\phi_k} \right\|. \tag{5}$$

Then, we replace the amplitude and phase of the DOE in each pixel by those with the smallest distance to the constrain modulation curve:

$$\text{DOE}[i,j] \rightarrow \text{MC}[k'], \tag{6}$$

where k' is the grey level of the MC closest to $A_{ij}e^{i\phi_{ij}}$. Therefore, after defining the seed with random phase and the target amplitude, a whole iteration of the proposed algorithm covers the following steps (see Fig. 2):

1st: Determine the transmittance of the DOE, $\text{DOE}[i,j] = A_{ij}e^{i\phi_{ij}}$, using the IFFT.

2nd: Calculate the distance between the field of the DOE, DOE$[i,j]$, respect to the field of each point of the constrain MC$[k]$, according to Eq. (5).

3rd: For each DOE's pixel, replace the amplitude and phase (A_{ij}, ϕ_{ij}) by the nearest value of the constrain modulation curve $(A_{k'}, \phi_{k'})$, according to Eq. (6).

4th: Propagate the new DOE to the image plane using the FFT and replace the amplitude, A', by the target's one, A_{target}.

We have implemented the proposed algorithm using the Python package Diffractio [27] (see supplementary material).

Our goal is to design complex modulation DOEs that fills the Argand plane as much as possible to minimize the average distances d_{ij}. However, we have to keep in mind that our complex DOEs will be limited by the constraint modulation curve of our system, MC$[k]$, defined by the polarization properties of the SLM and the polarization elements included in the set-up.

For the numerical simulations, we chose a spiral-shaped MC$[k]$ (shown in the upper left corner of Fig. 2), defined as

$$\text{MC}[k] = \frac{k}{K}e^{i\frac{k}{K}\gamma}, \tag{7}$$

since it fills the Argand plane by means of the γ parameter, which is the maximum phase shift of the spiral that determines the available phase variability of the MC. We have analyzed complex DOEs with spiral-shaped MC featuring different phase shifts. We have also simulated a pure-phase MC to compare our results with those of the standard IFTA. We studied the performance of several targets and, as an example, we showed the results obtained for a square flat-top. Fig. 3 displays the MC used in the D-IFTA (blue curves) along with the intensity pattern generated by the designed complex DOEs in the image plane. In the plots of the MCs, we have also shown the points that forms the Argand plane as black dots, whose size represents the minimum displacement to the MC. As γ increases, the distance between the Argand plane dots to the closest point of the MC is shorter and, therefore, the size of the black dots decreases. This performance is also shown in Figs. 3e and 3f, which display the decrease of the mean and maximum distances when increasing γ. On the other hand, the resulting flat-top using a $\gamma = 2\pi$ spiral-shaped MC (Fig. 3b) has more background noise respect to the pure-phase one. We think that it is due to the lack of symmetry of the spiral MC compared to the phase MC. However, the uniformity of the flat-top and the background level improve notably with spiral-shaped MCs with higher phase variability γ (Figs. 3c and 3d).

This improvement is also observed in Figs. 4 and 5. The first one shows the intensity profile of the resulting flat-tops using a pure-phase DOE and complex DOEs with spiral-shaped maps of $\gamma = 4\pi$, $\gamma = 8\pi$, and $\gamma = 16\pi$, respectively. Both intensity profiles, at $y = 0$ (Fig. 4a) and the average one (Fig. 4b) show that, as the MC fills the Argand plane, the flat-top fluctuations decrease. Fig. 5 shows the dependence of some quality parameters of the designed DOEs as a function of γ. As the seed of the IFTA is random, we have repeated the simulation 32 times for each γ value. Then, we have calculated their mean values (black dots of Fig. 5) and we performed an empirical fitting (black dashed line of Fig. 5), where the fitting functions are shown inside each subfigure. In addition, we have plotted the error bars of each mean value calculated as the standard deviation (STD) of the values obtained in the 32 simulations. It is shown that our algorithm is very robust from $\gamma = 3\pi$. Figs. 5a and 5b show the uniformity, measured as the STD, of the flat-top and background zones, respectively. In both cases, the STD drops sharply as γ increases from 2π to 4π and then, the STD decrease is smoother. The red dashed lines represent the STD of a pure-phase DOE, which reaches a value of 16.6% and 0.6% for the flat-top and background zones, respectively. However, a complex DOE with $\gamma = 8\pi$ already achieves standard deviations of 6% and 0.2%, showing the enhancement of complex DOEs compared to phase ones. Finally, we have calculated the diffraction efficiency of the obtained intensity patterns, defined as the fraction of the total power in the image plane falling into the flat-top region Ω and can be expressed as

$$\kappa = \frac{\iint_{\Omega} I_f(x,y)dxdy}{\iint_{\Omega+\Omega_c} I_f(x,y)dxdy}, \tag{8}$$

where $I_f(x,y)$ represents the intensity in the image plane and Ω_c the region outside the flat-top. Fig. 5c shows the diffraction efficiency as a function of γ and it proves that a $\gamma = 5\pi$ spiral-shaped MC already exceeds the diffraction efficiency of 94.6% of a pure-phase DOE. Therefore, in view of these results, the use of complex modulation DOEs allows us to achieve intensity distributions more uniform, with less background

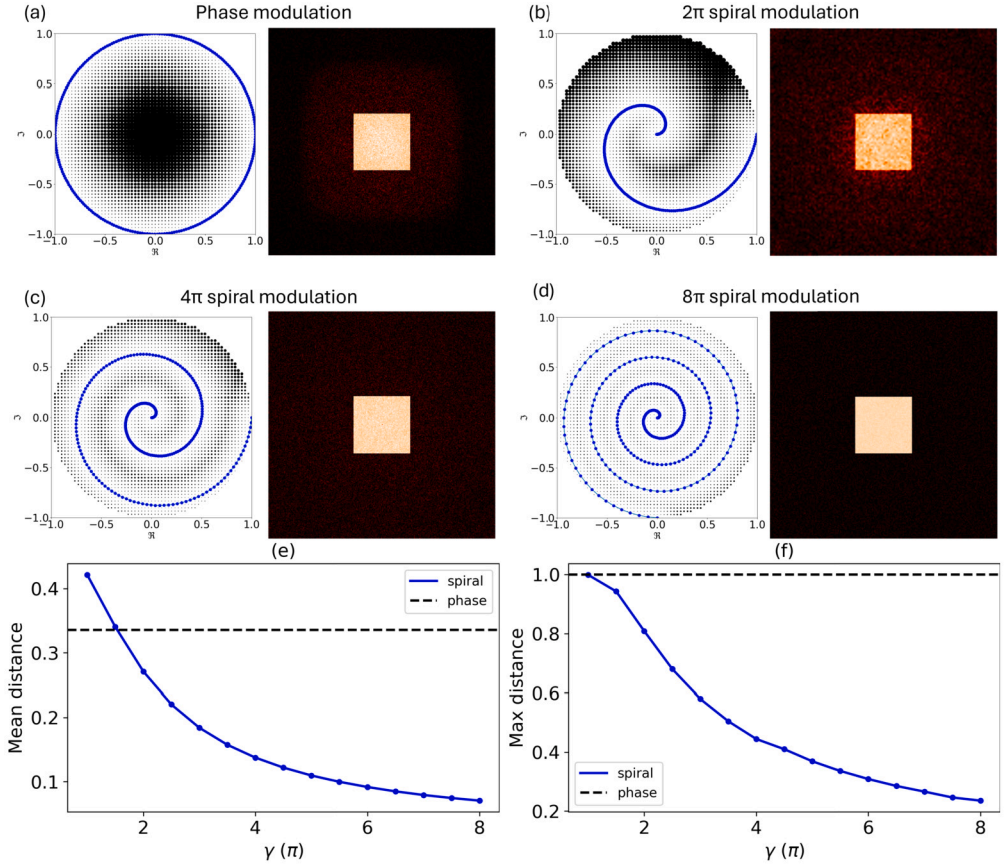

Fig. 3. Modulation curves for (a) a pure-phase DOE and spiral-shaped DOEs with (b) $\gamma = 2\pi$, (c) $\gamma = 4\pi$, and (d) $\gamma = 8\pi$, respectively. The points of the Argand plane are shown as black dots, whose size represents the minimum distance to the MC. The far-field diffraction pattern generated by each designed DOE is shown to the right of the MCs. We have used logarithmic scale in the intensity plots to enhance the influence of the background as γ increases. (e) Mean and (f) maximum distances between the points of the Argand plane and the spiral MCs, in terms of γ.

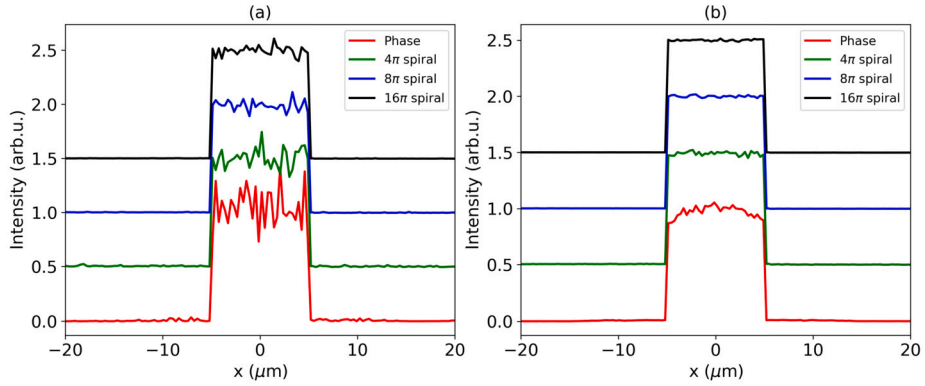

Fig. 4. (a) Normalized intensity profile at $y = 0$ and (b) normalized average intensity profile for the flat-tops generated by the designed DOEs. The profiles have been shifted along y-axis a value of 0.5 for their proper visualization.

noise and with higher diffraction efficiencies when we have enough phase variability.

4. Experimental results

We analyzed experimentally how the designed complex DOEs can be implemented with a single SLM. Fig. 6 shows the set-up used, which is also valid for measuring the Jones matrix of the SLM. A He-Ne laser, with a working wavelength of $\lambda = 632.8$ nm and a Gaussian beam profile (Melles Griot), is filtered and expanded using a ×40 microscope objective, a 10 μm pinhole and a collimating lens. Then, the light passes through a polarizer (P_0) and a quarter-wave plate (Q_0) to generate circularly polarized light. The beam is reflected in a mirror and goes through the PSG (P_1 and Q_1). Then, the beam passes through a 50:50 beam splitter (BS) which directs the light to the reflective SLM. We have used the PLUTO reflective LCoS modulator (Holoeye), which has a 1920 × 1080 pixels array and a pixel size of 8 μm × 8 μm. After the beam is reflected by the SLM, the light passes through the PSA (P_2 and Q_2), whose polarization plates are placed on RSW-E rotation motors (Zaber) like those of the PSG. Between Q_2 and P_2, we included a 4-f system ($f' = 100$ mm) that can be used to image the DOE generated on the SLM plane on a camera. We added a lens with a focal length $f' = 80$ mm to observe the far diffraction patterns of the DOE on the camera. In particular, we have used a 72BUC02-ML CMOS camera (Imaging Source Europe

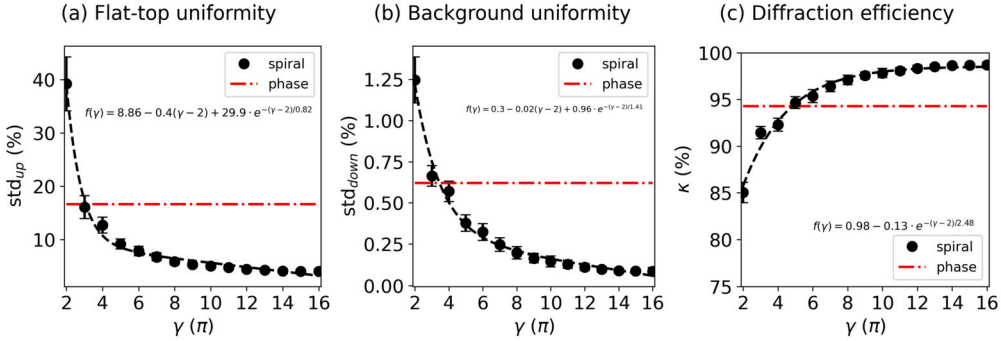

Fig. 5. Quality parameters of the designed complex modulation DOEs as a function of the maximum phase variability of the spiral-shaped MC, γ. Standard deviation of the (a) flat-top and (b) background, and (c) diffraction efficiency of the designed DOEs. The red dashed line represents the parameters values for a pure-phase DOE, while the black dashed line corresponds to the fit applied to the parameter values of the designed complex DOEs. Error bars are computed as the standard deviations of the parameters obtained for 32 different seeds of the D-IFTA.

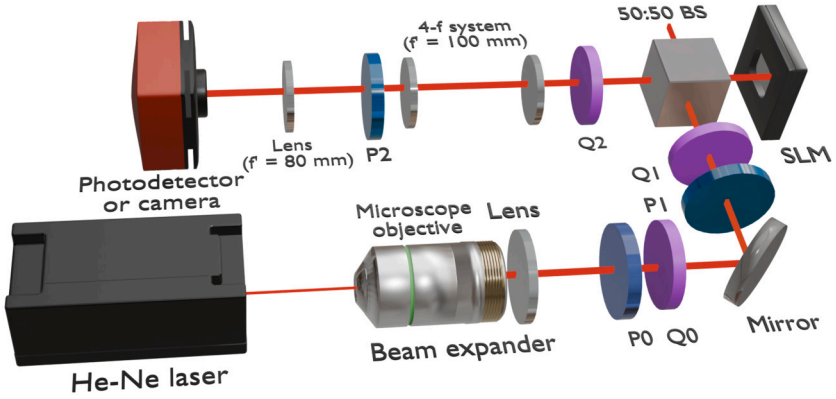

Fig. 6. Experimental set-up used to analyze complex modulation DOEs using a SLM. This set-up is also valid for determining the Jones matrix of the SLM. A He-Ne laser beam is filtered and expanded, and passes through a polarizer (P_0) and a quarter-wave plate (Q_0) to set its polarization to circular. The beam directs to the PSG (P_1 and Q_1) and, then, to a beam splitter in order to illuminate the SLM. The beam is reflected by the SLM and goes through the PSA (P_2 and Q_2) and a 4-f system to transfer the SLM plane. Finally, the light is captured by a camera to measure the far field distribution of the DOEs or focused on a photodetector to determine the Jones matrix of the SLM.

GmbH) with 2592 × 1944 pixels and a pixel size of 2.2 × 2.2 μm^2. On the other hand, to measure the Jones matrix of the SLM (see Eq. (1)), we have replaced the camera by a PDA100A2 photodetector (Thorlabs).

First, we have calibrated the SLM to optimize its MC. We have measured its Jones matrix, $\boldsymbol{J}_{SLM}$, which can be expressed as

$$\boldsymbol{J}_{SLM} = e^{i\phi} \begin{bmatrix} J_0 & J_1 e^{i\delta_1} \\ J_2 e^{i\delta_2} & J_3 e^{i\delta_3} \end{bmatrix}, \tag{9}$$

where J_l, $l = 0, ..., 3$, represents the amplitude of each matrix element, ϕ is the global phase, and δ_m, $m = 1, 2, 3$, corresponds with the difference between the phase of the m matrix element and the global phase. We obtained $\boldsymbol{J}_{SLM}$ using the procedure described in [28]. Fig. 7 shows the absolute values of the Jones matrix elements, the global phase and their phase differences over the 256 gray levels. It is worth noting that we have assumed spatial uniformity of the SLM. Although working under this assumption is not critical for the development of the proposed method, implementing calibration corrections to account for spatial non-uniformity, as reported in [29–31], would be beneficial.

Once we have calibrated our SLM, we calculated its real MC by multiplying the Jones matrices of the optical elements of our system as Eq. (1). For this purpose, we have used the Python open-source package Py-pol, which is focused on Jones and Stokes-Mueller polarization optics [32]. We must determine precisely the azimuth of the polarization elements (linear polarizers and retarders) according to the type of modulation we want to perform: amplitude, phase, or complex one. For that, we have used Particle Swarm Optimization (PSO) algorithm, a stochastic optimization algorithm where a group of agents explores the search space to find optimal solutions and whose positions improve iteratively based on their previous trajectories and evaluations of the Merit Function. In particular, we have used the Python open-source package PySwarms [33].

First, we have developed an optimization process to obtain a phase MC. In this case, we have defined a merit function (MF) that minimizes the amplitude variation and maximizes the phase variation of the emerging electric field of our set-up. We extracted the amplitude and phase of the output electric field and we defined the merit function for pure-phase modulation as

$$\mathrm{MF}_{\mathrm{phase}} = -\frac{\phi_{\max} - \phi_{\min}}{\mathrm{STD}(A)}, \tag{10}$$

where ϕ represents the phase and STD(A) is the standard deviation of the amplitude. Then, we perform other optimization process to obtain a complex MC. For this purpose, we have first defined a grid of points that covers evenly the normalized Argand plane, X_{grid}. Then, we have defined a MF that calculates the distance between the emerging amplitude-phase values of our set-up, i.e., the MC, and the defined grid. The merit function for complex modulation is expressed as

$$\mathrm{MF}_{\mathrm{complex}} = \frac{\sum_{i=0}^{N} \min \left\| X^i_{\mathrm{grid}} - X_{\mathrm{MC}} \right\|}{N}, \tag{11}$$

where X_{MC} represents the amplitude-phase values of our MC, N is the total number of points used in the defined grid, N = 317, which corresponds with the number of points in the Argand plane of Fig. 3, and $\|\cdot\|$ represents the distance at the complex plane. The function min(·) gives us the closest distance between the i point of the grid to one of the

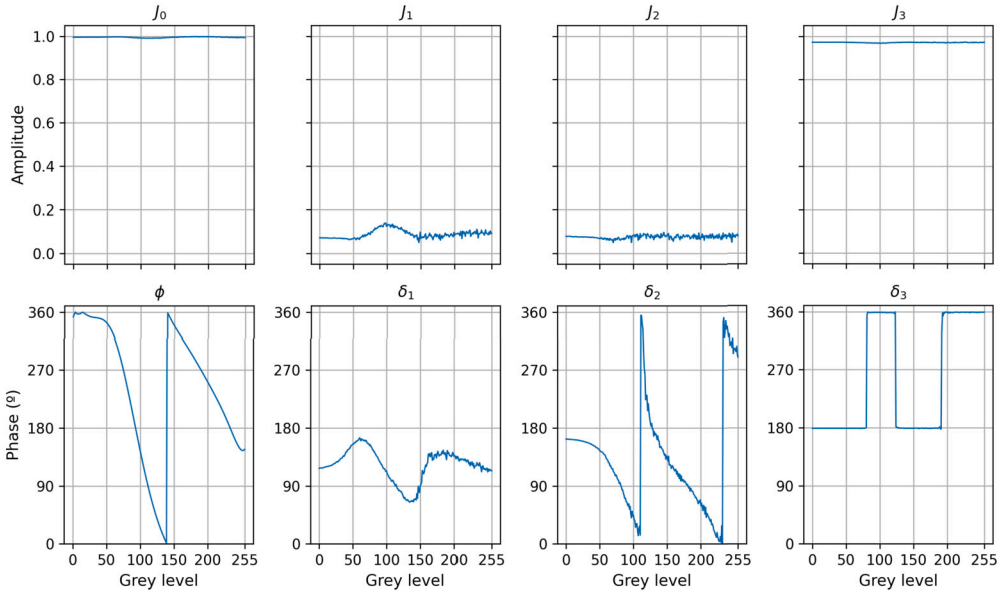

Fig. 7. Measured Jones matrix of the Holoeye Pluto SLM following the methodology of [28].

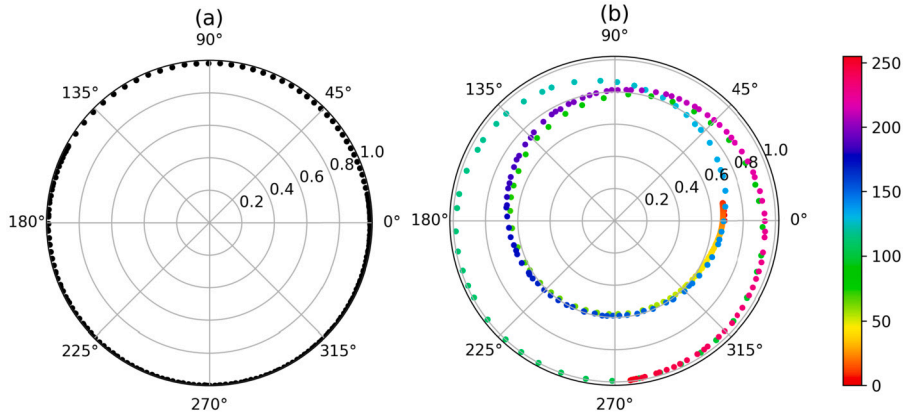

Fig. 8. MC for (a) phase and (b) complex modulation obtained with Particle Swarm Optimization algorithm. The colorbar of the complex MC shows the evolution of the curve as the gray level increases.

points of our MC. Using PSO, we minimize these distances and we try to fill the amplitude-phase space as much as possible.

For both phase and complex optimizations, we have to determine 4 parameters, the angular positions of the polarizers and quarter-wave plates of the PSG and PSA. We have used 50 particles, 100 iterations and we bounded the values between 0 and 180 degrees. After the optimization process, we obtained the following angles of the polarization plates $\vec{\theta^P} = \left(\theta^P_{P1}, \theta^P_{Q1}, \theta^P_{Q2}, \theta^P_{P2}\right) = (0.74°, 176.27°, 2.74°, 1.72°)$ for a phase modulation configuration and $\vec{\theta^C} = \left(\theta^C_{P1}, \theta^C_{Q1}, \theta^C_{Q2}, \theta^C_{P2}\right) = (134.02°, 110.64°, 109.90°, 91.01°)$ for a complex modulation configuration. The value of the merit function for the complex configuration, i.e. the average of the minimum distances between the MC and the defined grid, is $\mathrm{MF}_{\mathrm{complex}} = 0.271$. Fig. 8 shows the experimental phase and complex MCs, respectively. As usual, the phase modulation curve presents maximum transmission for all grey levels and a phase variability of 2π. On the other hand, the complex modulation curve has more phase variability, around 4π, and a minimum transmission of 0.6.

Once we have obtained the optimum MCs, we used them in the proposed D-IFTA to generate phase and complex DOEs and verify their performance using the SLM. First, taking into account the resolution and pixel size of our SLM, we defined a square flat-top as the target. Then, we generated the desired DOEs and grey level masks using D-IFTA. The main difference between DOEs and grey level masks is that the former is composed of the electric field values while the latter relates the electric field to the grey levels according to the MC used to sent it directly to the SLM. After generating the masks, we analyzed their performance using the set-up shown in Fig. 6. We rotated the polarization elements of the PSG and PSA to the angles obtained with the PSO, and we sent the generated mask to the SLM. Figs. 9a and 9b show the experimental diffraction pattern of a phase and complex DOE, respectively. The background noise significantly improves using the complex DOE. In fact, the background average value for phase modulation takes a value of 0.0781, while for complex modulation is 0.00932. Moreover, the complex DOE achieves a relative intensity of background noise of 5.48%, which is half the value reported in previous works [24]. We have also measured the uniformity of the background, calculated as the intensity STD, which decreases from 0.0227 to 0.0033, a reduction of ~85%. This enhancement is also shown in Figs. 9c and 9d, which represent the vertical average profile of the flat-tops for phase and complex modulation, respectively. In these profiles, we can clearly see that the background intensity uniformity and its mean value are lower for the complex DOE. We have also calculated the uniformity of the flat-tops from this average profiles, obtaining values of 0.0829 and 0.0708 for the phase and complex DOES, respectively, which corresponds to a reduction of ~15% (see Table 1). Finally, we calculated the diffraction efficiencies of both diffraction pat-

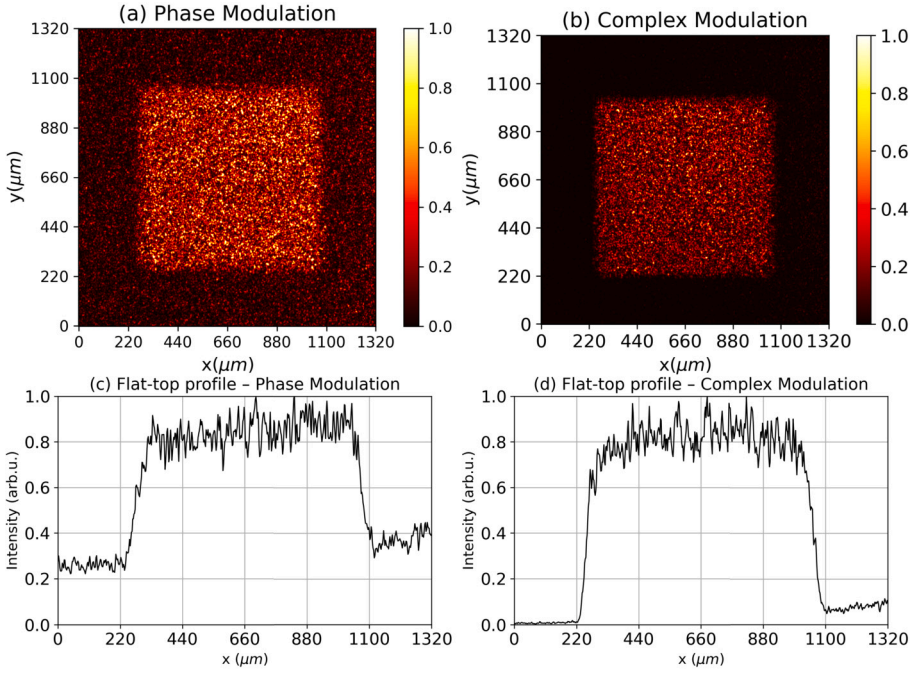

Fig. 9. Experimental far-field diffraction pattern for a (a) phase and (b) complex DOE, which generates a flat-top intensity pattern. Average vertical profile of the flat-top using (c) phase and (d) complex modulation.

Table 1
Intensity fluctuations, calculated as the standard deviation, of the diffraction patterns generated by phase and complex DOEs along with their diffraction efficiencies. The parameter STD_{up} corresponds to the intensity fluctuations of the flat-top, STD_{down} represents the background ones, and κ the diffraction efficiency (see Eq.(8)).

Parameter	Phase modulation	Complex modulation
STD_{up}	0.0829	0.0708
STD_{down}	0.0227	0.0033
κ (%)	68.61	90.85

terns, reaching a value of 68.61% for the phase DOE and a 90.85% for the complex DOE (see Table 1). The diffraction efficiency of the designed complex DOE represents an improvement in performance over other DOEs designed with modified IFTAs, as [15,17] reports diffraction efficiencies of around 85% and 70%, respectively. Therefore, although the phase variability of our SLM is not high, the improvement of using complex DOEs over pure-phase DOEs is already noticeable. Then, as shown in the previous section, these results could be potentially improved using a SLM which allows a higher maximum phase variability.

5. Conclusions

We have developed a technique to generate complex modulation DOEs implemented in a single Spatial Light Modulator. We have proven that, by using a SLM modulation curve that fills the Argand plane evenly, the performance of complex DOEs improves respect to pure-phase ones, since their far field diffraction patterns present less background noise and higher diffraction efficiencies. Moreover, this technique uses a much simpler set-up with fewer alignment problems than other methods. We have also proposed a distance-based IFTA algorithm to design complex DOEs in order to implement them in the SLM. This algorithm is based on the minimization of the average distance between the DOEs electric field delivered by each pixel and the modulation curve of the SLM. For the simulations, we have used spiral-shaped modulation curves. First, we numerically verified that, as the modulation curve is more evenly distributed in the amplitude-phase space, the performance of the complex DOEs increases. As an example, we designed complex DOEs that generate a flat-top intensity distribution in the image plane. The flat-top and its background uniformity, measured as the standard deviation of the intensity distribution in the region of interest, reduced from 16.6% and 0.6% for phase modulation to 7.48% and 0.3% using a $\gamma = 6\pi$ spiral-shaped modulation curve, respectively. For the experimental verification, we calibrated our SLM and we optimized the azimuths of the polarization plates of the PSG and PSA to fill the Argand plane as evenly as possible. We obtained a near $\gamma = 4\pi$ modulation curve, which is consistent with the maximum available phase shift of our SLM at $\lambda = 633$ nm. Finally, using this modulation curve, we designed complex DOEs that generate flat-tops at the image plane and we experimentally verified their performance. As in the simulations, one of the most noticeable improvements is the background noise. We obtain background uniformity values of 2.27% and 0.03% for the phase and complex DOEs, respectively. This means a reduction of 85% in background noise compared to the phase DOE. Moreover, the uniformity of the flat-top produced by the complex DOE, and its diffraction efficiency improves respect to the phase one a 15% and 30%, respectively. These results can be further enhanced by using SLMs with higher phase variability or shorter working wavelengths.

CRediT authorship contribution statement

Angela Soria-Garcia: Writing – review & editing, Writing – original draft, Visualization, Software, Methodology, Formal analysis, Data curation, Conceptualization. **Luis Miguel Sanchez-Brea:** Writing – review & editing, Supervision, Software, Project administration, Investigation, Funding acquisition, Formal analysis, Conceptualization. **Jesus del Hoyo:** Writing – review & editing, Supervision, Software, Investigation, Formal analysis. **Joaquin Andres-Porras:** Writing – review & editing, Visualization, Software, Investigation. **Javier Alda:** Writing – review & editing, Validation, Supervision, Project administration, Funding acquisition, Formal analysis.

Declaration of competing interest

The authors declare that they have no known competing financial interests or personal relationships that could have appeared to influence the work reported in this paper.

Acknowledgements

Authors acknowledge funding to “VDOEST” PID2022-138071OB-I00 project by MCIN/AEI/10.13039/501100011033/FEDER, EU and to “DISCREPO” PDC2023-145843-I00 project, funded by Ministerio de Ciencia, Innovación y Universidades. A. Soria-Garcia and J. Andres-Porras also acknowledge funding of a predoctoral fellowship from Universidad Complutense de Madrid and Banco Santander.

Appendix A. Supplementary material

Supplementary material related to this article can be found online at https://doi.org/10.1016/j.optlaseng.2025.109184.

Data availability

Data will be made available on request.

References

[1] Nikolenko V, Watson BO, Araya R, Woodruff A, Peterka DS, Yuste R. SLM microscopy: scanless two-photon imaging and photostimulation using spatial light modulators. Front Neural Circuits 2008;2. https://doi.org/10.3389/neuro.04.005.2008.

[2] Ham BS. A quantum spectrometer using a pair of phase-controlled spatial light modulators for superresolution in quantum sensing. arXiv:2405.08456, 2024.

[3] Otte E, Tekce K, Denz C. Spatial multiplexing for tailored fully-structured light. J Opt 2018;20(10):105606. https://doi.org/10.1088/2040-8986/aadef3.

[4] Franco E, Martínez-Matos Óscar, Rodrigo JA. Curve-shaped ultrashort laser pulses with programmable spatiotemporal behavior. Optica 2023;10(3):379–92. https://doi.org/10.1364/OPTICA.478086.

[5] Li X, Liu J, Jia J, Pan Y, Wang Y. 3D dynamic holographic display by modulating complex amplitude experimentally. Opt Express 2013;21(18):20577–87. https://doi.org/10.1364/OE.21.020577.

[6] Song Q, Baroni A, Sawant R, Ni P, Brandli V, Chenot S, et al. Ptychography retrieval of fully polarized holograms from geometric-phase metasurfaces. Nat Commun 2020;11:2651. https://doi.org/10.1038/s41467-020-16437-9.

[7] Arbabi A, Horie Y, Bagheri M, Faraon A. Dielectric metasurfaces for complete control of phase and polarization with subwavelength spatial resolution and high transmission. Nat Nanotechnol 2015;10. https://doi.org/10.1038/nnano.2015.186.

[8] Zhou S, Shen Z, Li X, Ge S, Lu Y, Hu W. Liquid crystal integrated metalens with dynamic focusing property. Opt Lett 2020;45(15):4324–7. https://doi.org/10.1364/OL.398601.

[9] Soria-Garcia A, del Hoyo J, Sanchez-Brea LM, Pastor-Villarrubia V, Gonzalez-Fernandez V, Elshorbagy MH, et al. Vector diffractive optical element as a full-Stokes analyzer. Opt Laser Technol 2023;163:109400. https://doi.org/10.1016/j.optlastec.2023.109400.

[10] Gerchberg RW. A practical algorithm for the determination of phase from image and diffraction plane pictures. Optik 1972;35:237–46.

[11] Wyrowski F, Bryngdahl O. Iterative Fourier-transform algorithm applied to computer holography. J Opt Soc Am A 1988;5(7):1058–65. https://doi.org/10.1364/JOSAA.5.001058.

[12] Hsu W-F, Lin S-C. Iterative pixelwise approach applied to computer-generated holograms and diffractive optical elements. Appl Opt 2018;57(1):A189–96. https://doi.org/10.1364/AO.57.00A189.

[13] Choi K, Kim H, Lee B. Synthetic phase holograms for auto-stereoscopic image displays using a modified IFTA. Opt Express 2004;12(11):2454–62. https://doi.org/10.1364/OPEX.12.002454.

[14] Zhang F, Cheng H, Zhang Q, Wei S. Phase retrieval using iterative Fourier transform and convex optimization algorithm. In: Javidi B, Son J-Y, editors. Three-dimensional imaging, visualization, and display 2015. Proceedings of SPIE, vol. 9495. International Society for Optics and Photonics; 2015. p. 949510.

[15] Zhang X, Chen G, Zhang Q. LCOS-SLM based intelligent hybrid algorithm for beam splitting. Electronics 2022;11(3). https://doi.org/10.3390/electronics11030428.

[16] Mikhaylov D, Zhou B, Kiedrowski T, Mikut R, Lasagni AF. Machine learning aided phase retrieval algorithm for beam splitting with an LCoS-SLM. In: Kudryashov AV, editor. Laser resonators, microresonators, and beam control XXI. Proceedings of SPIE, vol. 10904. Society of Photo-Optical Instrumentation Engineers (SPIE); 2019. p. 10 S., 47.01.02; LK 01. https://doi.org/10.1117/12.2508673.

[17] Li J, Zhang F, Pu M, Guo Y, Li X, Ma X, et al. Quasi-continuous metasurface beam splitters enabled by vector iterative Fourier transform algorithm. Materials 2021;14(4). https://doi.org/10.3390/ma14041022.

[18] Thomson LC, Courtial J. Holographic shaping of generalized self-reconstructing light beams. Opt Commun 2008;281(5):1217–21. https://doi.org/10.1016/j.optcom.2007.10.110.

[19] Khonina SN, Balalayev SA, Skidanov RV, Kotlyar VV, Päivänranta B, Turunen J. Encoded binary diffractive element to form hyper-geometric laser beams. J Opt A, Pure Appl Opt 2009;11. https://doi.org/10.1088/1464-4258/11/6/065702.

[20] Lima G, Neves L, Guzmán R, Gómez ES, Nogueira WAT, Delgado A, et al. Experimental quantum tomography of photonic qudits via mutually unbiased basis. Opt Express 2011;19(4):3542–52. https://doi.org/10.1364/OE.19.003542.

[21] Bordakevich S, Rebon L, Ledesma S. Optimization for maximum modulation of a double-pass twisted nematic liquid crystal display. Appl Opt 2022. https://doi.org/10.1364/ao.444721.

[22] Macfaden AJ, Wilkinson TD. Characterization, design, and optimization of a two-pass twisted nematic liquid crystal spatial light modulator system for arbitrary complex modulation. J Opt Soc Am A 2017;34(2):161. https://doi.org/10.1364/josaa.34.000161.

[23] Rosales-Guzmán C, Bhebhe N, Forbes A. Simultaneous generation of multiple vector beams on a single slm. Opt Express 2017;25(21):25697–706. https://doi.org/10.1364/OE.25.025697.

[24] Hasegawa S-y, Inoue H. High spatial resolution pixel synthesis structure for full-complex amplitude modulation with twisted nematic LCD. Appl Opt 2019;58(25):6725. https://doi.org/10.1364/ao.58.006725.

[25] Li Y, Zheng L, Caspary R, Roth B. Scalar far-field diffraction modelling using nonuniform fast Fourier transform for diffractive optical phase elements design. Opt Express 2025;33(1):1222–36. https://doi.org/10.1364/OE.540359.

[26] Runzhe Z, Siyuan Q, Yixiong L, Yinghui G, Xiaoyin L, Qi Z, et al. Structured-light 3d imaging based on vector iterative Fourier transform algorithm. Nanomaterials 2024;14(11). https://doi.org/10.3390/nano14110929.

[27] Sanchez-Brea LM, Soria-Garcia A, Andres-Porras J, Pastor-Villarrubia V, Elshorbagy MH, del Hoyo Muñoz J, et al. Diffractio: an open-source library for diffraction and interference calculations. In: Optics and photonics for advanced dimensional metrology III. Proceedings of SPIE, vol. 12997. International Society for Optics and Photonics; 2024. p. 129971B.

[28] del Hoyo J, Sanchez-Brea LM, Soria-Garcia A. Calibration method to determine the complete Jones matrix of SLMs. Opt Lasers Eng 2022;151:106914. https://doi.org/10.1117/12.2597156.

[29] Dai Y, Antonello J, Booth MJ. Calibration of a phase-only spatial light modulator for both phase and retardance modulation. Opt Express 2019;27(13):17912–26. https://doi.org/10.1364/OE.27.017912.

[30] Tiwari V, Gautam SK, Naik DN, Singh RK, Bisht NS. Characterization of a spatial light modulator using polarization-sensitive digital holography. Appl Opt 2020;59(7):2024–30. https://doi.org/10.1364/AO.380572.

[31] Kumar P, Nishchal NK. Phase response optimization of a liquid crystal spatial light modulator with partially coherent light. Appl Opt 2021;60(35):10795–801. https://doi.org/10.1364/AO.439654.

[32] del Hoyo J, Sanchez-Brea LM, Soria-Garcia A. Open source library for polarimetric calculations Py-pol. In: Computational optics 2021. International society for optics and photonics, vol. 11875. SPIE; 2021. p. 1187506.

[33] Miranda LJ. Pyswarms: a research toolkit for particle swarm optimization in Python. J Open Source Softw 2018;3(21):433. https://doi.org/10.21105/joss.00433.